NeuroImage 176 (2018) 454–464

Contents lists available at ScienceDirect

NeuroImage

journal homepage: www.elsevier.com/locate/neuroimage

Sub-millimeter ECoG pitch in human enables higher fidelity cognitive neural state estimation

John Hermiz [a], Nicholas Rogers [b], Erik Kaestner [c], Mehran Ganji [a], Daniel R. Cleary [d], Bob S. Carter [d], David Barba [d], Shadi A. Dayeh [e,f], Eric Halgren [g,h], Vikash Gilja [a,*]

[a] Department of Electrical and Computer Engineering, University of California San Diego, La Jolla, CA 92093, USA
[b] Department of Physics, University of California San Diego, La Jolla, CA, 92161, USA
[c] Neurosciences Program, University of California San Diego, La Jolla, CA, 92096, USA
[d] Department of Neurosurgery, University of California San Diego, La Jolla, CA, 92103, USA
[e] Department of Nanoengineering, University of California San Diego, La Jolla, CA, 92093, USA
[f] Department of Materials Science and Engineering, University of California San Diego, La Jolla, CA, 92093, USA
[g] Department of Radiology, University of California San Diego, La Jolla, CA, 92103, USA
[h] Department of Neurosciences, University of California San Diego, La Jolla, CA, 92103, USA

ARTICLE INFO

Keywords:
microECoG
Human
Machine-learning
PEDOT
Electrode
Language

ABSTRACT

Electrocorticography (ECoG), electrophysiological recording from the pial surface of the brain, is a critical measurement technique for clinical neurophysiology, basic neurophysiology studies, and demonstrates great promise for the development of neural prosthetic devices for assistive applications and the treatment of neurological disorders. Recent advances in device engineering are poised to enable orders of magnitude increase in the resolution of ECoG without comprised measurement quality. This enhancement in cortical sensing enables the observation of neural dynamics from the cortical surface at the micrometer scale. While these technical capabilities may be enabling, the extent to which finer spatial scale recording enhances functionally relevant neural state inference is unclear.

We examine this question by employing a high-density and low impedance 400 μm pitch microECoG (μECoG) grid to record neural activity from the human cortical surface during cognitive tasks. By applying machine learning techniques to classify task conditions from the envelope of high-frequency band (70–170Hz) neural activity collected from two study participants, we demonstrate that higher density grids can lead to more accurate binary task condition classification. When controlling for grid area and selecting task informative sub-regions of the complete grid, we observed a consistent increase in mean classification accuracy with higher grid density; in particular, 400 μm pitch grids outperforming spatially sub-sampled lower density grids up to 23%. We also introduce a modeling framework to provide intuition for how spatial properties of measurements affect the performance gap between high and low density grids. To our knowledge, this work is the first quantitative demonstration of human sub-millimeter pitch cortical surface recording yielding higher-fidelity state estimation relative to devices at the millimeter-scale, motivating the development and testing of μECoG for basic and clinical neurophysiology as well as towards the realization of high-performance neural prostheses.

Introduction

Recent advances in device engineering and human neurophysiology has stimulated interest in recording electrical activity from the surface of the brain, a technique referred to as Electrocorticography (ECoG). Current studies have demonstrated that ECoG probe features can be shrunk to sub-mm scales (μECoG) with devices that have remarkable substrate flexibility allowing the probes to conform to the surface of the brain (Castagnola et al., 2015; Ganji et al., 2017; Insanally et al., 2016; Kellis et al., 2009; Khodagholy et al., 2016, 2014; 2011; Toda et al., 2011;

Abbreviation: HFB, high frequency band; ACC, classification accuracy; ELR, elastic-net logistic regression; STG, superior temporal gyrus; CAR, common average reference; MVN, Multivariate normal.

* Corresponding author.
E-mail address: vgilja@ucsd.edu (V. Gilja).

https://doi.org/10.1016/j.neuroimage.2018.04.027
Received 2 November 2017; Received in revised form 9 March 2018; Accepted 11 April 2018
Available online 18 April 2018

Trumpis et al., 2017). Novel devices also demonstrate the integration of flexible electronics on these substrates, which could result in a new generation of ultra-high density probes with 1,000s to 10,000s of electrodes (Fang et al., 2017; Viventi et al., 2011). New methods for applying organic materials, in particular poly(3,4-ethylenedioxythiophene) doped with polystyrene sulfonate (PEDOT:PSS), have yielded relatively low impedance (Ganji et al., 2017; Khodagholy et al., 2014, 2011) electrodes with areas as small as 10 μm^2 (Khodagholy et al., 2016), enabling electrophysiology with high signal fidelity. These proof of concept technologies have enabled neurophysiologists to discover novel neural dynamics from the surface of the brain, including recurrent spiral waves manifested from seizures in animal model (Viventi et al., 2011) and single unit activity in both animal model and studies in the clinic (Khodagholy et al., 2016, 2014). These developments could lead to advances in basic neuroscience research and medical applications such as clinical mapping and brain-machine interfaces (Blakely et al., 2008; Bleichner et al., 2016; Branco et al., 2016; Chang, 2015; Ganji et al., 2017; Hwang and Andersen, 2013; Jiang et al., 2017; Kaiju et al., 2017; Kellis et al., 2010; Leuthardt et al., 2009; Maharbiz et al., 2017; Muller et al., 2016b).

A major question raised in the advancement of device technology is, "How dense should surface grids be?" There is likely no universal answer to this question, since relevant parameters are application dependent and, in particular, the spatial characteristics of neural activity could vary between cortical regions and functional settings. Previous simulation and empirical studies have used spatial spectral techniques to estimate the ideal spacing to be 1.25 mm (Freeman et al., 2000; Slutzky et al., 2010). Other empirical works have quantified spatial characteristics by using similarity metrics such as channel correlation vs channel distance (Chang, 2015; Insanally et al., 2016; Kellis et al., 2016; Muller et al., 2016b; Trumpis et al., 2017) with the interpretation that steeper falloffs indicate that high density grids are advantageous. However, a well-defined functional interpretation of these falloff curves has not been established. In this work, we develop an illustrative model to gain an intuition for how spatial signal and noise properties affect the performance gap between high and low density grids from a machine learning perspective. Furthermore, we apply this perspective to examine sub-millimeter pitch grid recordings from the human cortical surface.

Typical adult clinical ECoG probes have an interelectrode spacings ("pitch") of 1 cm, and research grids with pitches as low as 30 μm have been used intraoperatively (i.e. Neurogrid) (Chang, 2015; Khodagholy et al., 2016, 2014). Previous electrophysiology studies demonstrated that grids with pitches below 1 cm capture richer electrophysiology, and a number of research studies employ "HD-ECoG" grids with 3–4 mm pitch that are manufactured by the same companies with the same processes and materials as standard adult clinical grids (Chang, 2015; Flinker et al., 2011; Flint et al., 2017; Wang et al., 2016). However, the anatomic organization of cortex motivates the exploration of higher resolution probes. Anatomically, much of the cortex seems to be organized into mini-columns with a diameter of ~50μ, and functional columns have been identified in various sensory and motor systems with varying diameters, often ~400μ (Horton and Adams, 2005; Rockland, 2010). However, there is great variability across species and areas, and in particular columns have never been demonstrated in human associative cortex (Horton and Adams, 2005; Rockland, 2010). Previous works have demonstrated sub-mm probes can capture novel electrophysiological detail on micro-meter scale (Ganji et al., 2017; Kaiju et al., 2017; Khodagholy et al., 2016, 2014; Viventi et al., 2011). In human studies of sub-millimeter pitch ECoG grids, recorded signals are evaluated using measures of electrophysiological signal similarity (e.g. correlation, coherence) (Insanally et al., 2016; Kellis et al., 2016; Muller et al., 2016b; Trumpis et al., 2017). While these measures provide insight into potential utility of higher density recordings, they do not provide a direct connection into the potential of higher spatial resolution devices to more accurately estimate neural state. Evaluating changes in functionally relevant neural states is crucial both for basic neurophysiology studies and for the development of neural prosthetic devices. Although neural state is an abstract concept, we can consider a concrete instantiation of neural state by utilizing cognitive tasks to drive areas of interest towards different states (eg. hearing human voice vs noise). Then we apply machine learning algorithms to evaluate if the additional views of neural state provided by higher resolution recording improves our ability to classify task conditions from neural activity alone. In this work, we compare the classification accuracy of 400 μm, 800 μm, and 1200 μm pitch grids from two subjects. Intraoperative recordings were made with a 400 μm grid and has electrodes arranged in a 7 × 8 grid with an electrode diameter of 50 μm (Fig. 1B). The electrodes were coated with PEDOT:PSS, which facilitates higher signal to noise ratio recording from small area electrodes than conventional metal electrodes (Ganji et al., 2017; Khodagholy et al., 2011). Subjects were engaged in audio-visual tasks, where multiple classes of time-locked stimuli were presented and classified based on neural signal features. We generated 800 μm, and 1200 μm pitch "virtual" grids by sub-sampling the 7 × 8 grid similar to Muller et al., who suggests that 2 mm can outperform 4 mm and 8 mm grids (Muller et al., 2016a). In this work, we evaluate grids with 25x the density of this previous study while also adding controls for channel count and coverage area (Fig. 1C). Similar work was also performed in rats with 200 μm pitch grid (Ledochowitsch et al., 2013) and in monkey with 700 μm pitch grid(Kaiju et al., 2017), albeit with differing analyses that may not directly translate to humans. Here, we show that 400 μm spaced grids can significantly outperform 800 μm and 1200 μm when controlling for coverage area.

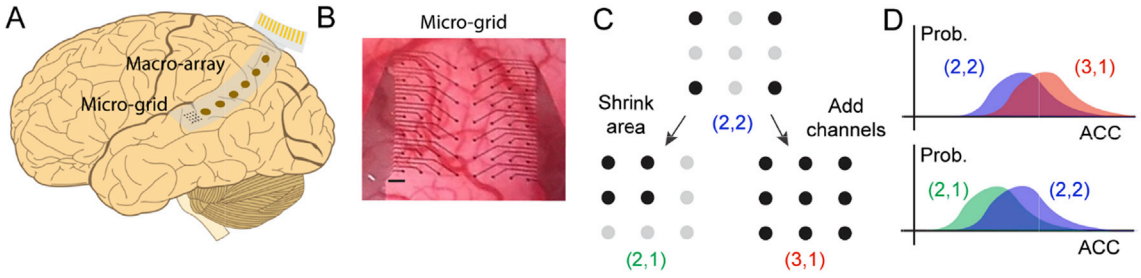

Fig. 1. High density, μECoG assessment. (A) Sketch of the surface probe used in this work which can record both μECoG (56 electrodes) and ECoG (6 electrodes). Note the actual μECoG is smaller than depicted. The yellow strips indicate the only other exposed conductive region, in which a conductive film will be bonded for interfacing with the device. B) Picture of implanted μECoG probe used in this work, which was manufactured using micro/nano-fabrication techniques. The electrodes are arranged is a 7 × 8 grid with a pitch of 400 μm, a diameter of 50 μm, and coated with PEDOT:PSS. The scale bar is 400 μm. (C) Drawing depicting two ways to increase electrode density: shrink area or add more channels for a given area. By sub-sampling electrodes from the grid, we can determine if increasing density can be beneficial. The notation (2,2), for example, means a 2 × 2 grid with twice the pitch spacing. The benefit is defined to be higher decoding accuracy of audio-visual stimuli presented to the subject. (D) Sketch comparing hypothetical distribution of accuracies from different probability densities with the same area (top) and different spacing with fixed channel count (bottom).

Table 1
Commonly used symbols.

Symbol	Description	Symbol	Description
σ_s	characteristic length for signal	$\boldsymbol{s}$	signal across channels
λ	characteristic length for noise	$\boldsymbol{\Sigma}$	channel co-variance matrix
a	signal amplitude for center channel	d^2_{m}	squared Mahalanobis distance
$\boldsymbol{x}$	measurements across channels	Δ	difference in squared Mahal. distance

Methods

Please refer to Table 1 for commonly used symbols used throughout the text.

Modeling

Description

To explore when higher density grids might outperform (or underperform) comparable lower density grids, a model was developed and studied under various circumstances. Let $\boldsymbol{x}$ be a d-dimensional measurement or feature vector of real numbers, where d is the channel count. In general, $\boldsymbol{x}$ is assumed to include signal and additive noise.

$$\boldsymbol{x} = \boldsymbol{s} + \boldsymbol{n} \tag{1}$$

Two conditional random variables are defined $\boldsymbol{x_p} = \boldsymbol{x}|c = p$ and $\boldsymbol{x_{np}} = \boldsymbol{x}|c = np$, where c denotes the class a particular feature vector belongs to: p (preferred stimuli) or np (non-preferred stimuli). We will assume only the preferred stimuli has signal. Previous studies have shown that correlation between raw channels measurements and features derived from various frequency bands can fit reasonably well to an exponential decay (Insanally et al., 2016; Kellis et al., 2016; Muller et al., 2016b; Trumpis et al., 2017). This motivated defining the signal to decay exponentially with respect to Euclidean distance from the peak activation site.

$$s_i = a^* \exp\left(-\frac{||r_i - r_{ctr}||}{\sigma_s}\right) \tag{2}$$

Note, r_i is the position of the *ith* channel and r_{ctr} is the position of the channel with peak (or center) activation. a scales the magnitude of signal and, as will subsequently become evident, is the signal to noise ratio (SNR) for the center channel. σ_s is the characteristic length for the signal, which is when $||r_i - r_{ctr}|| = \sigma_s$ corresponding to a $1/e \approx 0.37$ decrease in the signal. For simplicity, the noise is assumed to be Gaussian with zero mean and unit variance ($\Sigma_{ii} = 1$), $\boldsymbol{n} \sim N(0, \boldsymbol{\Sigma})$; hence, SNR, which is defined to be the mean divided by the standard deviation for the center channel is a. Again, it is assumed that noise covariance decays exponentially as a function of distance. Here, λ is the characteristic length of noise correlation. So, two electrodes that are spaced λ units apart from each other will have a correlation of $1/e \approx 0.37$.

$$\Sigma_{ij} = \exp\left(-\frac{||r_i - r_j||}{\lambda}\right) \tag{3}$$

The overall model can be rewritten as

$$\boldsymbol{x_p} \sim N(\boldsymbol{s}, \boldsymbol{\Sigma}) \tag{4}$$

$$\boldsymbol{x_{np}} \sim N(0, \boldsymbol{\Sigma}) \tag{5}$$

Analysis

This simple, yet plausible model allows us to explore situations in which higher density grids outperform lower density grids. We are mainly interested in two comparisons: 1) fix area and vary channel count (or equivalently pitch) and 2) fix channel count and vary pitch (or equivalently area). In order to compare grids, we need a metric. Since $\boldsymbol{x_p}$ and $\boldsymbol{x_{np}}$ are drawn from multivariate normal distributions with the same covariance matrix, the natural choice is the Mahalanobis distance, d_m between the means of the distributions.

$$d_m^2 = \boldsymbol{s}^T \boldsymbol{\Sigma}^{-1} \boldsymbol{s} \tag{6}$$

In fact, researchers in related work have used the Mahalanobis distance to score "evoked signal-to-noise ratio" in trials indicating that these assumptions are reasonable (Insanally et al., 2016; Trumpis et al., 2017). Intuitively, $\underline{d_m}$ is the average separation between feature vectors from the preferred and non-preferred stimuli. The larger the separation, the more discriminable the two classes of data are. What we are interested in is how that separation changes as a function of grid density. That is, the difference or difference squared,

$$\Delta = d^2_{m,hd} - d^2_{m,ld} \tag{7}$$

To gain an intuition for when higher density grids have an advantage, we compute analytical expressions for Δ in the two-channel case: 1) the difference between two vs one channel, $\Delta_{2,1}$ and 2) the difference between two channels that are 1 unit apart vs 2 units apart, $\Delta_{2,2'}$.

$$\Delta_{2,1} = \frac{(s_2 - s_1\Sigma_{21})^2}{1 - \Sigma_{21}^2} \tag{8}$$

$$\Delta_{2,2'} = \frac{(s_2 - s_1\Sigma_{21})^2}{(1 - \Sigma_{21}^2)} - \frac{(s_{2'} - s_1\Sigma_{2'1})^2}{(1 - \Sigma_{2'1}^2)} \tag{9}$$

See Sections A4.1-A4.2 for derivation. As is obvious from Eqns (8) and (9), there is a singularity when $\Sigma_{21} = 1$ or $\Sigma_{2'1} = 1$. This occurs because the squared Mahalanobis distance, $d^2_{x_1,x_2}$ or $d^2_{x_1,x_2'}$ cannot be computed as $\det(\boldsymbol{\Sigma})$ becomes undefined and $\boldsymbol{\Sigma}$ uninvertible. This likely never occurs in practice as there is always measurement noise that is not perfectly correlated across channels.

Time series

A simple time series extension of the spatial model is described. The measurement vector, $\boldsymbol{x}$ that has d elements for the number of channels becomes a matrix, $\boldsymbol{X}$ that is d x T, where T is number of time samples. Again, we will assume in general that the signal is deterministic and that there is additive noise.

$$\boldsymbol{X} = \boldsymbol{S} + \boldsymbol{N} \tag{10}$$

In the non-preferred condition, $\boldsymbol{S} = 0$ and in the preferred condition $\boldsymbol{S} = \boldsymbol{F}$ where $\boldsymbol{F}$ are samples for a set of deterministic functions that evolve over space and time. The rows of $\boldsymbol{F}$ are denoted $\boldsymbol{f}_1, \boldsymbol{f}_2, .. \boldsymbol{f}_d$. As before, the signal on each channel decays exponentially with distance from the center channel, $\boldsymbol{x_{ctr}}$ which we will set to be $\boldsymbol{x_1}$.

$$\boldsymbol{f}_j = \boldsymbol{f}_1 \exp\left(\frac{-||r_1 - r_j||}{\sigma_s}\right) \tag{11}$$

The time evolution of $\boldsymbol{f}_1$ is assumed to follow a Gaussian shape where the peak activation occurs at t_{pk}.

$$\boldsymbol{f}_1 = a \exp\left(\frac{-||t - t_{pk}||}{\sigma_t}\right) \tag{12}$$

Finally, the noise matrix $\boldsymbol{N}$ are just T copies of the original model's random variable $\boldsymbol{n}$, so that it's entries across time are independent and identically distributed. Hence, the noise spatial relationship of Eqn (3) still holds.

Probe

The probe used in experiments consists of 56 μECoG and 6 ECoG electrodes. The μECoG electrodes are arranged in a 7×8 grid with a 400 μm pitch and an electrode diameter of 50 μm. The ECoG electrodes are arranged is a strip or line spaced 1 cm apart with an electrode diameter of 3 mm. The μECoG were used to record surface potentials while the most of the ECoG electrodes were tied to reference. A stainless steel needle probe was used for ground and was inserted into the scalp at the edge of the craniotomy. The electrodes are coated with an organic conducting polymer called poly(3,4-ethylenedioxythiophene) doped with polystyrene sulfonate (PEDOT:PSS). PEDOT:PSS has been shown to reduce impedance values by orders of magnitude compared to traditional metal electrodes (eg. Pt). The typical electrode impedance magnitude at 1 kHz is 13 kΩ. Lastly, the substrate is 4–5 μm thick parylene which can conform to the surface of the brain. Additional device details can be found in (Ganji et al., 2017; Uguz et al., 2016). The data acquisition system used is described extensively in (Hermiz et al., 2016) and briefly in Section A.1.

Sub-sampling

The 7×8 grid of electrodes was sub-sampled to obtain "virtual" grids. There are many ways to sub-sample and an exhaustive enumeration of all possible sub-samples is not only intractable, but would be challenging to interpret. Since we are interested in determining if certain grid densities are beneficial we chose to limit all virtual grids to be square as these virtual grids could easily be parameterized and related to electrode density.

Virtual square grids can be parameterized by 3 variables (ignoring electrode size): number of channels, pitch (or spacing), and the area that the grid encompasses. If pitch is normalized to take on integer values (1, 2, …), then we can relate the variables using the following expression: $A = (p(\sqrt{c} - 1)^2$, where A, p and c are the area, pitch and number of channels, respectively. We explored the device parameter space by fixing each variable for a given analysis and changing the other degree of freedom: fixed pitch (Fig. 6), fixed area (Fig. 7), and fixed channel count (Fig. S7). We are primarily interested in comparing virtual devices with fixed area (Fig. 7).

Since our grid contained bad recording channels, we only considered virtual grids that had at least 50% of the channels they were supposed to have. For example, let's say a 5×5 grid had 13 good recording channels (52%), then the virtual grid would not be thrown out; however, it had 12 good recording channels (48%), then the virtual grid would be thrown out.

In some situations, it might be the case that a grid with 50% good electrodes is compared to a grid with 90% good electrodes, in which case the percentage of good channels confounds the comparison. To ensure there our results were not biased by the confounding variable of percentage of good channels, we performed a meta-analysis where we found the difference in percentage of good channels for all comparisons and determined if the distributions were significantly biased away from 0. We did not find a significant bias for the fixed area comparison, but did find a bias for the fixed channel comparison for SD007 (Fig. S8). We discuss the interpretation of the fixed channel comparison results in light of this bias in the Discussion and Section A.9.

Machine learning

Features were computed by summing up the HFB for each channel in non-overlapping windows of 0.25 s. For SD007, the start and end time were 0.15 and 0.9 s post stimulus onset and for SD008, the start and end time were 0.5–1 s post stimulus. Elastic-net logistic regression (ELR) was used to classify presented stimuli types. ELR was used because it is robust to high dimensional datasets and generally yields competitive classification accuracies (Zou and Hastie, 2005). ELR is a regularized version of logistic regression. It uses a combination of ridge (L_2-penalty) and lasso (L_1-penalty) regularization to reduce and eliminate the effect of non-discriminatory features. Ultimately, the result in a linear discriminate that should have few, high magnitude weights. The ELR implementation used was Glmnet Toolbox for Matlab (Qian et al., 2013). The mix of L_1 and L_2 penalty was fixed to be 0.75 and 0.25, while the weight of the regularization penalty was chosen by sweeping through 50 candidate values 12 times (for 12-fold cross validation) and choosing the value that maximizes the average accuracy. Aggregate accuracy statistics are computed from validation sets.

Experimental task

Subjects SD007 and SD008 undergoing clinical mapping of eloquent cortex provided informed consent to have the probe placed on their pial surface and to participate in a 10-min task. The μECoG grid was placed on the left superior temporal gyrus (STG): anterior STG for SD007 and posterior STG for SD008. UC San Diego Health Institutional Review Board (IRB) reviewed and approved study protocol.

The preferred and non-preferred categories were assigned by visually inspecting the trial averages of the high frequency band envelope. The category that yielded the largest response was labeled preferred while the category that yielded the smallest or no response was labeled non-preferred.

SD007 read visual words (e.g text of the word 'lion'), repeated auditory words (eg. audio of the word 'lion'), and named visual pictures (eg. picture of a 'lion'). The stimuli that elicited the largest response was the auditory word, therefore it was labeled preferred. Both visual pictures and words yielded little if any response. Visual words were chosen to be in the analysis and were labeled non-preferred. It is expected that the auditory word elicits the largest response since the probe was implanted on STG, which is responsible for auditory processing. There were 60 auditory word trials and 59 visual word trials analyzed in this study.

SD008 saw a 3-letter string (GUH, SEE) and then heard an auditory 2-phoneme combination, making a decision whether the visual and auditory stimuli matched. Interspersed were visual control trials in which a false font was followed by a real auditory stimulus and auditory control trials in which a real letter string was followed by a 6-band noise-vocoded 2-phoneme combination. For SD008, binary classification was performed between noise-vocoded stimuli and human voice. In these recordings, the noise-vocoded stimuli produce a larger response than human voice and therefore the noise-vocoded was labeled preferred while human voice was labeled non-preferred. This is consistent with previous work examining cognitive processing and evoked responses to noise-vocoded and human voice in posterior STG (Travis et al., 2013). There were 68 noise-vocoded trials and 63 human voice trials analyzed in this study.

Results

Modeling and experimental analyses were performed to determine if and when higher density grids outperform lower density grids. An illustrative model with properties motivated from previous studies (Insanally et al., 2016; Kellis et al., 2016; Muller et al., 2016b; Trumpis et al., 2017) was developed to determine under what conditions a higher density grid might outperform a lower density grid. Analytical results for the simple 2-channel case and numerical results for higher dimensional cases are presented (Fig. 2). We then analyze real μECoG recordings acquired from two subjects, SD007 and SD008 engaged in audio-visual tasks in the operating room. Two types of stimuli were classified and classification accuracy served as the performance metric when comparing grids. Sub-sampling the 7×8 grid allowed us to explore the device design space and, in particular, electrode density.

Modeling

We developed a simple model that assumes measurements belong two

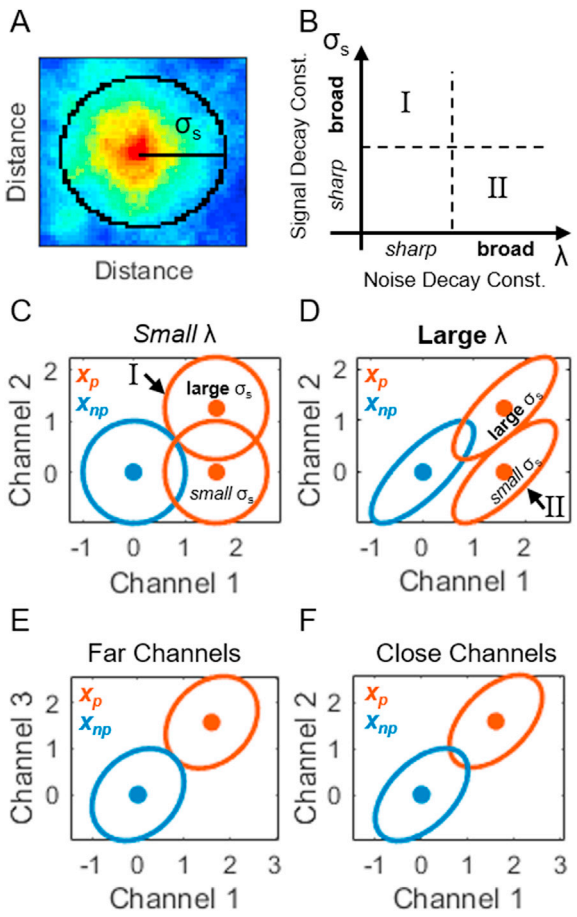

Fig. 2. Multivariate normal (MVN) model parametrized by decaying exponentials. (A) Spatial representation of signal fall-off length σ_s (arbitrary units) using generated data from the model. Note, that dark red maps to the maximum value and dark blue maps to the minimum value. For more visualizations of signal and noise fall-off length, λ see Fig S1 (B) Illustration of which regions in the parameter space σ_s - λ where higher density grids outperform lower density grids. There are two regions: I, σ_s is large and λ is small or II, σ_s is small and λ is large. (C–F) 2-channel feature space where the MVN for various random variables are plotted – dots are means and the ellipses are 1 standard deviation. The distribution of channel measurements from the non-preferred stimulus, $\boldsymbol{x_{np}}$ are blue and the distribution from the preferred stimulus, $\boldsymbol{x_p}$ are red. (C) Illustrates effect I: given a small λ, a larger σ_s will increase separation between $\boldsymbol{x_{np}}$ and $\boldsymbol{x_p}$. Note small λ corresponds to little correlation and thus a circular distribution. (D) Illustrates effect II: given a large λ, a smaller σ_s will increase separation. Note large λ corresponds to large correlation and thus a skewed distribution along the $y = x$ axis. (E–F) Illustrates when 2 channels spaced far apart (low density) can be better than when spaced close together (high density). In this case, σ_s must be large and λ must be relatively small.

types of stimuli, preferred, $\boldsymbol{x_p}$ and non-preferred, $\boldsymbol{x_{np}}$ and are generated from multivariate normal (MVN) distributions: $\boldsymbol{x_p} \sim N(\boldsymbol{s}, \boldsymbol{\Sigma})$ and $\boldsymbol{x_{np}} \sim N(0, \boldsymbol{\Sigma})$. The signal of interest, $\boldsymbol{s}$ is assumed to peak at a specific electrode, x_{ctr} and fall off exponentially with a characteristic length, σ_s. In all analyses, the electrode x_{ctr} is a member of all grids and is the center most electrode. When there is an even number of electrodes, then x_{ctr} is the left center most electrode. Please note that in these simulations, the peak location of the signal is not modeled as randomly related to electrode location, as would be the case in actual recordings. Had our model permitted response peaks between electrodes, then tight electrode spacing would be highly advantageous, inasmuch as it would make it more likely that the response peak would be directly measured. However, for the current work, we only focus on the case where the peak activation is on the grid and is centered. The results from this condition can be viewed as a highly conservative estimate of how advantageous high-density grids are.

Noise correlation is also modeled as a decaying exponential with characteristic length, λ. That is, electrodes closer together will have more correlations whereas channels farther apart will have less. Here, noise can be interpreted as baseline neural activity that is independent of the stimulus.

The assumption that signal and noise decay exponentially across space is supported by existing studies that fit similarity measures of raw and band-limited signals to exponential decay functions with little error (Muller et al., 2016b; Trumpis et al., 2017). The squared Mahalanobis distance is used to measure the separation between the mean value of $\boldsymbol{x_p}$ and $\boldsymbol{x_{np}}$, $d_m^2 = \boldsymbol{s}\boldsymbol{\Sigma}^{-1}\boldsymbol{s}$ and the difference in the squared Mahalanobis distances of two grid configurations is denoted Δ. Larger absolute Δ values indicates that one grid configuration enables the acquisition of neural signals that better distinguish the preferred and non-preferred stimulus. The sign of Δ indicates which of the two grids is advantageous – by convention, $\Delta > 0$ means that higher density is more advantageous.

Analytical

To gain intuition for when higher density grids might enhance state estimation, we find analytical expressions for the difference of squared Mahalanobis distances, generally denoted as Δ, in the two-channel case. $\Delta_{2,1}$ is defined as the difference between two vs one channels and $\Delta_{2,2'}$ is the difference between two channels spaced two vs one units apart. The analytical expressions for $\Delta_{2,1}$ and $\Delta_{2,2'}$ are given in Eqn (8) and Eqn (9), respectively. $\Delta_{2,1}$ is never negative since, as expected, there is never an advantage of using only 1 channel vs 2 channels. Another intuitive finding is that the minimum of $\Delta_{2,1}$, which is 0, is reached when the signal is the same on both channels, $s_1 = s_2$ and the noise correlation, Σ_{12} approaches 1 (see Section A4.3). That is, when the measurements on both channels becomes equal, the value of recording from both channels vs just one vanishes. On the other hand, $\Delta_{2,1}$ and $\Delta_{2,2'}$ are large when either: I) σ_s is large and λ is small II) σ_s is small and λ is large (Fig. 2B). These effects are illustrated in Fig. 2C–D. In Fig. 2C, a sharp fall-off of the characteristic noise length (small λ) results in noise that is almost uncorrelated and isotropic, or equivalently the iso-probability density contour is circular. Depicted in blue and red are the non-preferred, $\boldsymbol{x_{np}}$ and preferred measurements, $\boldsymbol{x_p}$, respectively. In Fig. 2C, there are two cases in which the preferred measurements are plotted: small (sharp fall-off) and large (broad fall-off) σ_s. When σ_s is small, the preferred measurements will fall close to the x-axis, but when σ_s is large, they will fall towards the $x = y$ line. Larger σ_s results in more separation between non-preferred and preferred points by up to a factor of $\sqrt{2}$. Intuitively, effect I) can be thought of as enhancing SNR by averaging measurements with the same signal, but uncorrelated noise. Effect II is illustrated in Fig. 2D. Here, λ is large resulting in high correlation among the channels and thus an oblong iso-probability density contour. Again, measurements where σ_s is small and large are considered. When σ_s is large, the iso-contours representing 1 standard deviation have some overlap; however, when σ_s is small, that overlap is eliminated as the Mahalanobis distance between the non-preferred and preferred points increases (Fig. 2D). Unlike $\Delta_{2,1}$, $\Delta_{2,2'}$, the difference of the squared Mahalanobis distance between two channels spaced 1 and 2 units apart, can be negative meaning that in some cases there is a disadvantage to having electrodes spaced close together when comparing grids with the same number of electrodes. This can occur if the signal on both channels is almost the same (σ_s is large) and when correlation between channel 1 and 2' decays significantly compared to channel 1 and 2 (λ is about equal to the pitch) (Fig. 2E–F).

Lastly, SNR scales the advantage or disadvantage of high density electrodes. So, if there is an advantage to higher density as is likely to be the case for $\Delta_{2,1}$, then increasing SNR will enhance that advantage. However, it would also enhance the disadvantage of higher density when $\Delta_{2,2'} < 0$. This can be seen by factoring out a from $\boldsymbol{s}$ in Eqn (6), which

shows that $d_m^2 \propto a^2$ and thus $\Delta \propto a^2$. This SNR scaling effect is true for the general d-channel case.

Numerical

To determine whether the effects found in the analytical expressions of the 2-channel case generalized to higher dimensional cases, the 25-channel results were numerically computed from Eqn (6). Again, two comparisons were made: 1) fixed area, comparing a 5×5 grid with unit pitch vs a 3×3 grid with twice unit pitch and 2) fixed channel count, comparing a 3×3 grid with unit pitch vs a 3×3 grid with twice unit pitch. The difference in squared Mahalanobis distances for 1) and 2) will be denoted as $\Delta_{5,3'}$ and $\Delta_{3,3'}$, respectively.

As expected, SNR scales the difference in performance $\Delta_{5,3'}$ and $\Delta_{3,3'}$. In Fig. 3A, both $\Delta_{5,3'}$ and $\Delta_{3,3'} > 0$ for $\sigma_s = 0.5$ and $\lambda = 1$, so increasing SNR increases the difference in squared Mahalanobis distance quadratically. Interestingly, Fig. 3B shows for $\sigma_s = 10$ and $\lambda = 1$ high density provides an advantage or disadvantage depending the comparison: $\Delta_{5,3'} > 0$ and $\Delta_{3,3'} < 0$. Hence, SNR quadratically increases $\Delta_{5,3'}$ and decreases $\Delta_{3,3'}$. These results follow directly from our analytical findings described in the last paragraph of Section 3.1.1.

Consistent with the effects found in the analytical expressions of the 2-channel case, there are two regions in σ_s-λ space where higher density outperforms: I) $\sigma_s < 1$ and $\lambda > 1$ or II) $\sigma_s > 1$ and $\lambda < 1$ for $\Delta_{5,3'}$ and $\lambda < 1/3$ for $\Delta_{3,3'}$ (Fig. 3C–D). As anticipated from our 2-channel analytical results, there is a region where higher density underperforms when comparing grids with the same channel count, which is roughly $\sigma_s \gg 1$ and $1/2 < \lambda < 2$. Finally, as expected, $\Delta_{5,3'} > 0$ for all computed values in the domain $0.1 \leq \sigma_s, \lambda \leq 10$, or, simply put, the 3×3 grid with twice unit spacing never outperforms the 5×5 grid with 1 unit spacing for all the parameters we used.

Time series

It is important to note that the presented model has no notion of time, but simple extensions can be made to model time. One extension is to have the signal evolve according to a Gaussian function and assume the noise is independent and identically distributed across time (see Section 2.1.3 for explicit definition). An important statistic often computed from high density recordings is the correlation between two channels vs the distance between those channels. The correlation between the center channel, $\boldsymbol{x_1}$ and any other channel $\boldsymbol{x_j}$ is (see Section A4.4 for derivation)

$$\rho_{x_1 x_j} = \frac{(\Sigma_{1j} + \alpha_j p - \mu_1 \mu_j)}{\sqrt{\Sigma_{11} + p - \mu_1^2}\sqrt{\Sigma_{jj} + \alpha_j^2 p - \mu_j^2}} \qquad 13$$

where $\alpha_j = \exp\left(\frac{-||r_1 - r_j||}{\sigma_s}\right)$, $\Sigma_{1j} = \exp\left(-\frac{||r_1 - r_j||}{\lambda}\right)$, $p = E[\boldsymbol{f}_1^2]$, $\mu_1 = E[\boldsymbol{x}_1]$ and $E[\boldsymbol{x_j}] = \mu_j$. Numerical calculations suggested out that $\rho_{x_1 x_j} \approx \Sigma_{1j}$ when SNR in $\boldsymbol{x_1}$ is not too large (Fig. S2). That is, if the SNR is not too large, then the channel correlation computed from the time series of this model, will be approximately equal to the entries of the noise covariance matrix. Under these circumstances, we can extend the results of the spatial model to this time series model. This is important because we can interpret commonly computed correlation vs distance plots using our framework.

Empirical

Next, we explore the advantages of higher density grids by analyzing real μECoG recordings from two subjects intraoperatively at UC San Diego, Thornton Hospital. The grid has 7×8 micro-electrodes spaced 400 μm apart and a diameter of 50 μm. These subjects were engaged in an audio-visual task (see Section 2.5). Various types of time locked stimuli were presented to the subjects and stimuli class served as ground truth for offline neural state decoding experiments. For each subject, there were 2

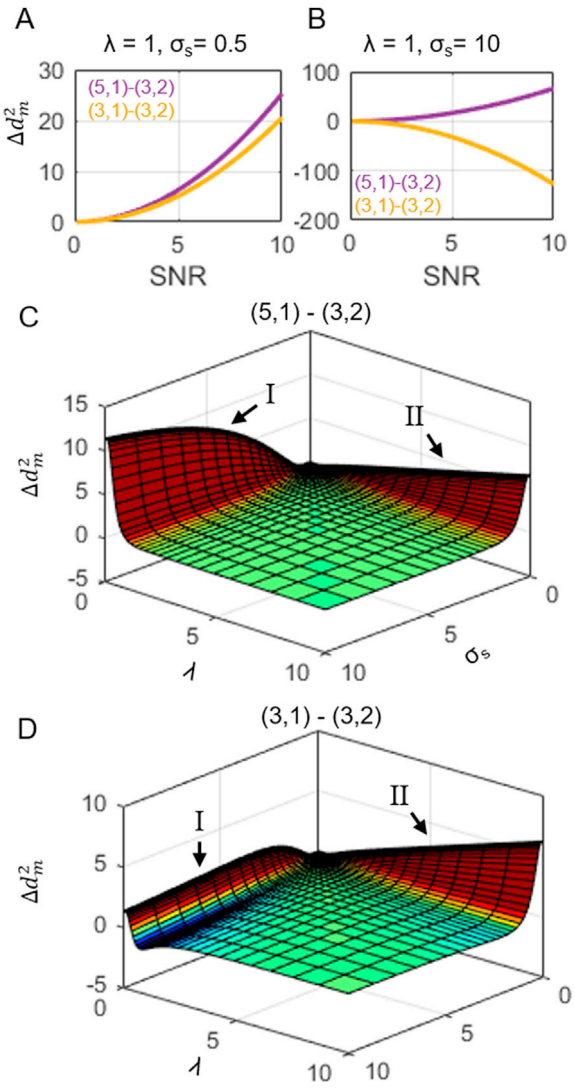

Fig. 3. (A–D) Numerical results from (5,1) vs (3,2) and (3,1) vs (3,2). The notation (a,b) refers to a grid that has a by a channels and has a pitch of b. (A–B) As SNR increases, the difference of squared Mahalanobis distance (Δd^2_m) increases or decreases, depending on σ_s, λ and which grids are compared. (C–D) 3d plots showing Δd^2_m for a grid of σ_s and λ values. (C) For (5,1) – (3,2), there are no values for which $\Delta d^2_m < 0$, given the domain; and as expected, $\Delta d^2_m \gg 0$, when σ_s, is large and λ is small or vice versa. (D) For (3,1) - (3,2), $\Delta d^2_m < 0$, when roughly, $\sigma_s > 5$ and $1 < \lambda < 2$, which is expected. Again, $\Delta d^2_m \gg 0$ when σ_s, is large and λ is small or vice versa. The color axis ranges from −1 (dark blue) to 1 (dark red) and is used to represent sign.

stimulus classes classified: one that produced a marked neural response and one that did not. Rectified high frequency band (70–170 Hz) amplitude (HFB) was used to measure the neural response because it has been shown to have high spatial specificity and correlation with sensory and cognitive processing (Crone et al., 1998; Miller et al., 2007). Fig. 4A–C shows how the raw trials were processed to yield HFB (Section A.2). The trials were then parsed into 0.25 s windows and summed to compute the features (Section 2.4).

The spatial spread of HFB activation was qualitatively assessed by taking the peak HFB in time and using cubic interpolation across space (Fig. 4D–G). The plots for each subject are normalized to indicated the percentage of the peak response. For both subjects, there is a clear region where the activation is markedly larger. For SD007, the highly-activated region appears to be confined to a smaller area and the dynamic range is larger than SD008. The preferred and non-preferred stimuli were

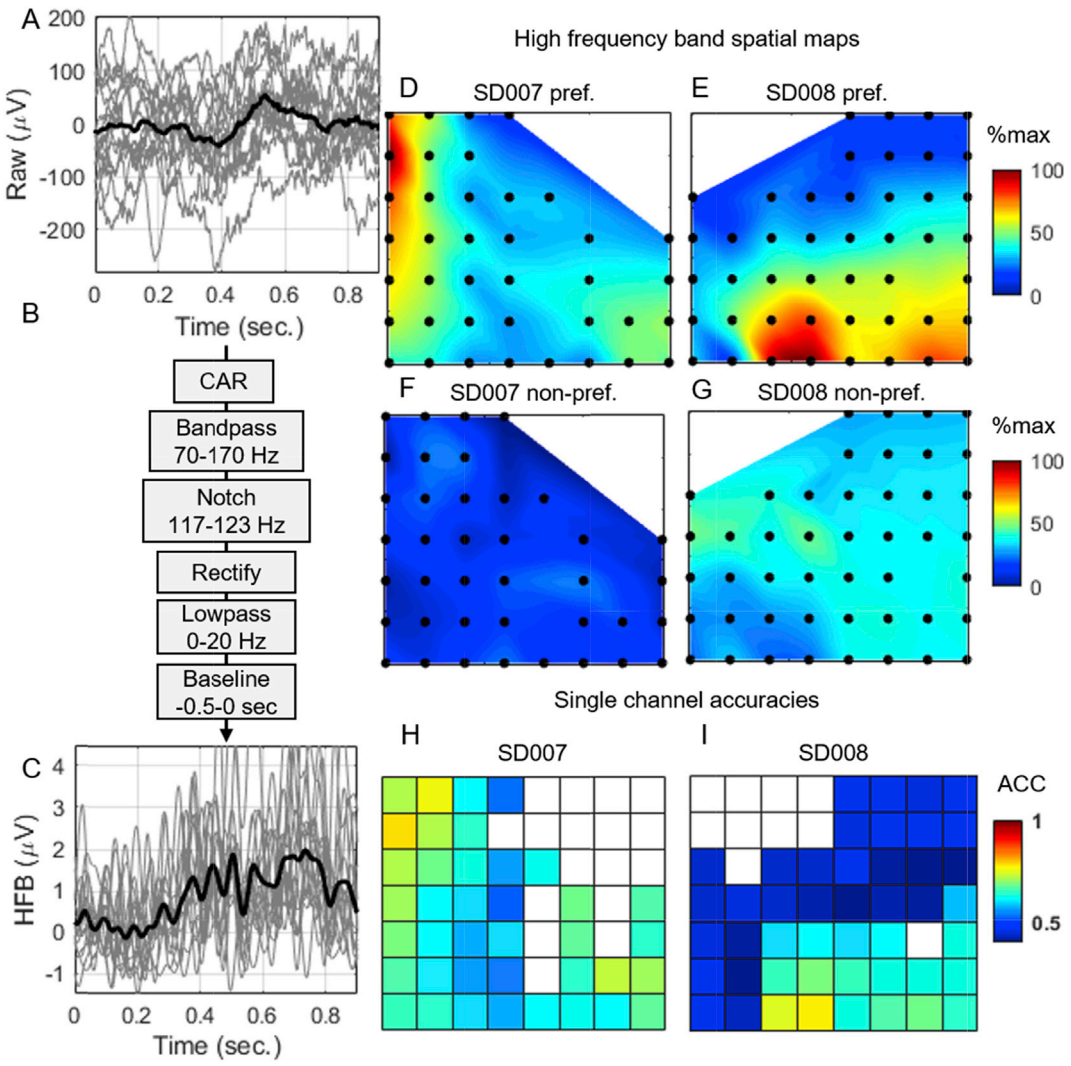

Fig. 4. Signal processing pipeline. (A) Trials of raw measurements (no post processing) shown in gray and the trial average is shown as black (B) Block diagram of signal processing (C) Trials of high frequency band (HFB) activity shown in gray and the trial average is shown as black. Cubic interpolation across space of peak HFB due to preferred stimuli (D) SD007 and (E) SD008 vs non-preferred stimuli (F) SD007 and (G) SD008. Units are percent of maximum response across stimuli type for each subject. White space could not be interpolated due to lack of channels. Single channel ACC for (H) SD007 and (I) SD008. White squares indicate thrown out channels.

classified by applying the HFB features to Elastic Net Logistic Regression (ELR) – a classification algorithm robust to high dimensional datasets with a limited number of examples (Qian et al., 2013; Zou and Hastie, 2005) (Section 2.4). The single channel classification accuracy (ACC) results are consistent with the heatmaps of the HFB activation (Fig. 4H–I). Maximum single channel ACC for SD007 and SD008 is 78% and 77%, respectively. Note, chance performance is 50% since classification is between two labels.

A common technique for removing interference (eg. movement artifact, electromagnetic interference) in EEG/ECoG is common average referencing (CAR), where the average of the raw measurements across all channels is subtracted for each channel (Crone et al., 2001; Ludwig et al., 2009). After applying CAR, the trial averaged HFB for each channel was more prominent and smoother for SD008, while SD007 did not change much suggesting that there was substantial interference for SD008 (Figs. S3–S4). Re-doing the HFB heatmaps with CAR changed the spatial activation to be more focal and increased the dynamic range for both subjects (Fig. 5A–D). While the classification results did not change very much for SD007, SD008 saw a dramatic increase in single channel ACC across all channels (Fig. 5E–F). Maximum single channel decoding after CAR is 77% and 89% for SD007 and SD008, respectively. Interestingly, in SD008 a block of channels in the upper-right portion of the grid jumped from among the worst to best classifying electrodes. Since in this work we sub-sample the grid, we defined CAR_{ss}, which uses only the sub-sampled channels to compute the average. On the other hand, it is important to identify whether using all the channels in the average, denoted CAR_{tot}, would improve interference removal, since the additional parallel recordings may result in a more accurate estimate of common noise. Note CAR_{ss} is the same as CAR_{tot} when all channels are sampled. ACC across square virtual grids with unit pitch, but varying number of channels (or coverage area) for all possible placements were computed. As channel count (or coverage area) increases, the general trend, irrespective of which CAR method was used, is that the median ACC increases (Fig. 5G–H), which will be highlighted shortly. When fitting a linear mixed effects model where CAR methods and channel count were fixed effects and fold-location-channel count was the random effect, an increase in ACC was observed when applying CAR_{tot} or CAR_{ss} vs No CAR. When comparing CAR_{tot} vs No CAR, there was a 3.0% and 5.8% difference in ACC for SD007 and SD008, respectively. When comparing CAR_{ss} vs No CAR, there was no significant difference for SD007, but there was a significant difference for SD008 at 6.2%. Note, the linear mixed effects model was fit for data points that ranged from 9 to 56 channels. The

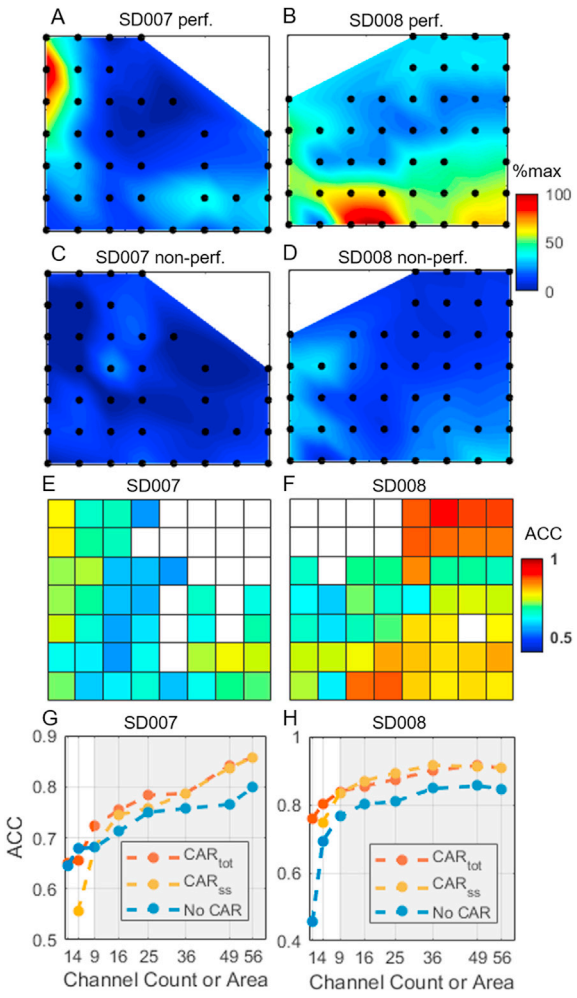

Fig. 5. Common average referencing (CAR) can improve ACC. HFB spatial maps after doing CAR using all kept channels. Preferred stimuli for (A) SD007 and (B) SD008 vs non-preferred stimuli (C) SD007 and (D) SD008. Single channel accuracy after CAR (E) SD007 and (F) SD008. Median of the mean accuracy vs channel count (or coverage area) using minimum pitch sub-sampled grids. The mean is taken over 12 cross validation folds and the median is taken over different virtual grid placements in that order. The 3 sets are: using all channels to do CAR (CAR_{tot}), only channels that were sub-sampled (CAR_{ss}), and no CAR. A linear mixed effects model was fit for data points that have 9 to 56 channels as indicated by the shaded gray region in (G–H). The fixed effects were CAR type and channel count while the random effect was fold-location-channel count. (G) For SD007, there was a 3.0% ($p < 1e\text{-}3$, $n = 1980$) increase when applying CAR_{tot} compared to No CAR, but an insignificant increase when applying CAR_{ss} compared to No CAR. (H) For SD008, there was a 5.8% ($p < 1e\text{-}3$) difference when applying CAR_{tot} compared to No CAR, and a 6.2% ($p < 1e\text{-}3$) difference for CAR_{ss} compared to No CAR ($n = 2448$).

effect on CAR_{tot} can also be seen on the HFB trial averages Figs. S3–S4. As expected, CAR_{tot} appears to greatly reduce interference in the trial averages for SD008, while in SD007 there is no obvious difference. To be consistent with the sub-sampling paradigm, we use CAR_{ss} for all subsequent analyses unless stated otherwise.

Do larger virtual grids with fixed density do better? To address this question, we sub-sampled square grids with unit pitch as depicted in Fig. 6a. We summarized the performance of each class of virtual grids by taking the mean ACC across cross validation folds and then either the median or maximum across all virtual grid placements. Fig. 6B–C shows these summary statistics plotted against channel count. When considering the median (red dots) performing grid across placements, there is a significant positive correlation of 1 and 0.86 for subjects SD007 and SD008, respectively. When considering the best placed grid (blue), there was significant correlation with channel count of 0.88 for SD007; however, the difference in ACC is only 10% (max) compared to 30% (median). There was no correlation for the max case in SD008. These results indicate that larger virtual grids with fixed density improves performance in general. Grids placed in the ideal location outperform the median performing grid, but less so as the grid size grows.

Does adding more electrodes within a given area improve performance? This is one way to determine if higher density is beneficial. To determine this, higher density grids were sub-sampled and ACC statistics were compared (Fig. 7a). The notation (3,1) refers to a 3×3 grid with unit pitch and (3,1) – (2,2) means that (3,1) has it's ACC statistics subtracted from (2,2), a 2×2 grid with twice unit pitch. The top two performing high density placements were only used for each comparison in Fig. 7B–C. The mean ACC difference across 12 cross-validation folds and two placements ($n = 24$) was computed between the high and low density grids (Table 2). Histograms of the pairwise ACC differences are shown in Fig. 7B–C. For SD007, higher density appeared more advantageous with 400 μm pitch grid significantly outperforming 800 μm or 1200 μm pitch grids by more than 10% 3 out 4 comparisons, whereas in SD008, 400 μm pitch grids significantly outperformed by 5–10% 2 out 4 comparisons ($p < 0.01$ Wilcoxon signed rank test). It is important to note that SD008 is closer to the ceiling of maximum performance, which may explain why there is smaller improvement (Table 2). Across both subjects, all mean differences between grids of different densities but the same area were positive suggesting that it's never detrimental to use a higher density grid with the same footprint. This result is consistent with intuition and our modeling results.

Discussion

The central question we explored in this work is "do higher density grids convey a benefit for neural state decoding?" We demonstrated empirically from intraoperative human electrophysiology data, obtained from cortical surface μECoG while two subjects were awake and engaged in an audio-visual task, that neural state estimation is improved with increased spatial resolution. Furthermore, we formulated a model with simple, yet informed assumptions to explore when higher density might outperform lower density.

In the model, we explored how signal spread (σ_s) and noise spread (λ) among channels affect the difference in performance between high and low density grids? Using the model, we derive expressions for the difference in performance (squared Mahalanobis distance) in the 2-channel case and numerically compute it in the 25-channel case. Taken together, we find that there are two regimes where high density grids strongly outperform: I) σ_s small and λ is large or II) σ_s is large and λ is small. In words, this occurs when there I) is a focal spatial activation or II) when there is less correlated noise among neighboring channels, but not both. There is never a disadvantage in high density when the grid is directly sub-sampled within a given area, but there can be a disadvantage when channel count is fixed and electrodes are brought closer. It is counterproductive to bring channels closer together if the signal across space is broad and correlation among channels falls off considerably across space. To our knowledge, this is the first time a model has been demonstrated which relates basic channel statistics such as correlation among channels to a functionally relevant metric, classification performance. This is important because many studies primarily report empirical results such as channel correlation computed from time series as function of distance (Insanally et al., 2016; Kellis et al., 2016; Muller et al., 2016b; Trumpis et al., 2017), which alone can have limited and possibly misleading interpretations. A frequent assumption is that sharper falloff in channel correlation or other similarity metrics across distance indicates value in high density while a broad falloff indicates lack of value (Kellis et al., 2016; Muller et al., 2016b). This intuition is contradicted by the modeling results, which shows that a classifier using features from a high density grid can substantially outperform a low density grid even when

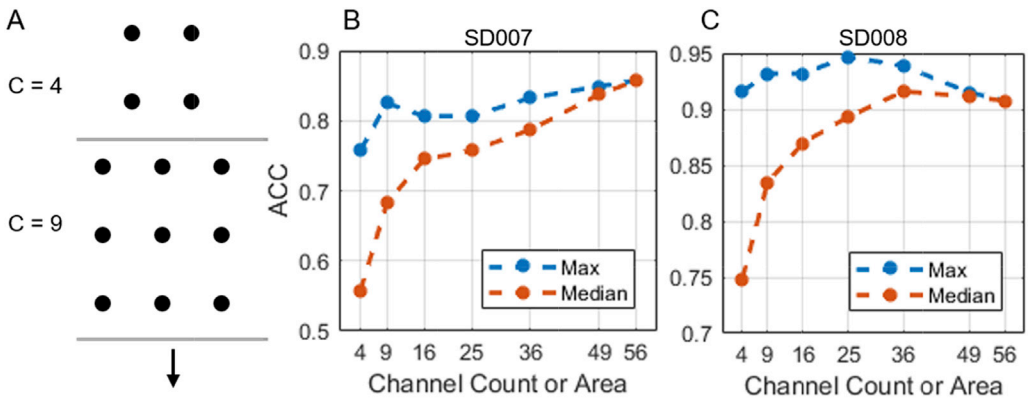

Fig. 6. Do larger virtual grids with fixed density do better? (A) Sketch showing the grids used in this analysis are square minimum pitch grids. (B) SD007 and (C) SD008 accuracy vs channel count (or coverage area) with two sets: max of mean (blue) and median of mean (red) across all possible sub-samplings of square grids. Note, chance is 50%. The mean is taken across 12 cross validation folds and the max or median is taken across different virtual grid placements. There is a significant Spearman correlation in (B) of 1 ($p < 1e\text{-}3$) and (C) of 0.86 ($p = 0.028$) for the median of mean data points with a difference of 30% and 15% in ACC from 4 to 56 channels. For the max of mean data points only SD007 showed a significant correlation (B) of 0.88 ($p = 0.015$) with a smaller difference in ACC of 10% from 4 to 56 channels.

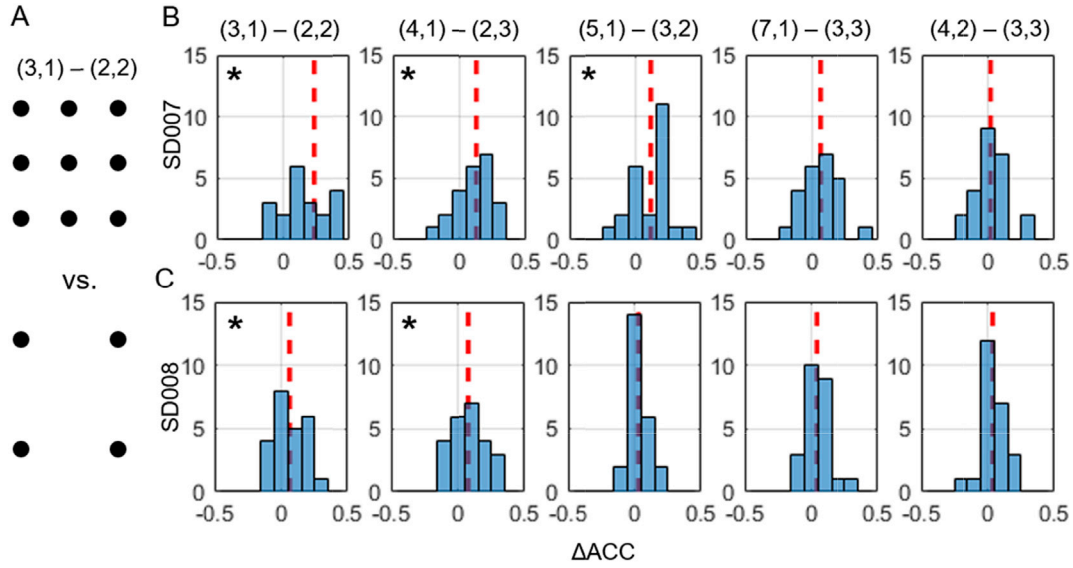

Fig. 7. Is adding more channels to a grid with fixed area coverage beneficial? (A) Sketch comparing two sub-sampled grid types with the same coverage area: 3×3 with minimum pitch (3,1) and 2×2 with double min. pitch (2,2). (B) SD007 and (C) SD008 histograms comparing various device types of the same coverage area. The x-axis of the histogram is pairwise difference (same location) of accuracy (ΔACC) between two devices types (eg. (3,1) and (2,2)). The two best high density grid locations were used and other locations were excluded. The notation (3,1) – (2,2) means accuracies of 3×3 min. pitch devices minus 2×2 double min. pitch devices. Distribution statistics are provided in Table 2. ACC sample vectors with significantly different mean ranks are denoted with a black asterisk ($P < 0.01$). The dashed red line indicates the mean of the pairwise differences.

there is high channel correlation (effect II). Insights made from modeling efforts, like those presented here, will likely be important for informing μECoG device design for scientific research, clinical mapping and brain-machine interface applications.

A limitation of the presented analyses is that placement was fixed and assumed to be ideal in all cases. That is, the peak activation occurred at the center of the grids. In real datasets, this need not be the case as illustrated from our own datasets (Figs. s.s. 4–5). This placement constraint can lead to counterintuitive results such as there is little performance gain from low to high density grids when both noise and signal decay rapidly. There is no performance gain because, the center channel picks up the same signal, while the surrounding electrodes pick up uncorrelated noise. In actual recordings the peak activation could be located off center or between electrodes where finer sampling would be advantageous to reduce the expected distance between peak activation and a nearest neighbor electrode. Since in the modeling work, we only focused on the case where the peak activation was centered, these results can be viewed as conservative or an underestimate of the advantages of high density grids. Analysis and simulations that look at various peak locations is important future work.

Another limitation of the model is that structure of the signal and noise is assumed to fall-off exponentially across space. Although studies have found that a decaying exponential models the fall-off of channels statistics across space well, the structure of the neural spatial response is likely to vary between cortical regions and with neural state. The neural response may take on multifaceted patterns with multiple sources organized sparsely in space, which motivates the use of high-density grids to finely sample the cortical surface. High-density grids may enable the development of more accurate models to capture the structure of neural response across space.

We found empirically that μECoG grids with 400 μm outperformed 800 μm and 1200 μm when controlling for area. Mean pairwise ACC differences were as large as 23.1% and appeared to be larger for SD007 compared to SD008 suggesting that higher density grids with the same

Table 2
Is adding more channels to a grid with fixed area coverage beneficial? Overall (fold + location) mean difference between paired accuracies, p-values from Wilcoxon signed-rank sum test (n = 24), and mean accuracy of the high-density grid. The mean difference of sample vectors which are significantly different from each other are denoted by **bold** ($P < 0.01$).

Comparison	SD007			SD008		
	Mean Δ	p-value	Mean HD	Mean Δ	p-value	Mean HD
(3,1) – (2,2)	**23.1%**	<1e-3	82.0%	**6.2%**	8.5e-3	92.8%
(4,1) – (2,3)	**12.5%**	1.4e-3	79.5%	**7.7%**	4.7e-3	92.4%
(5,1) – (3,2)	**11.3%**	1.6e-3	79.9%	3.1%	0.059	93.5%
(7,1) – (3,3)	6.3%	0.043	83.7%	4.1%	0.080	91.1%
(4,2) – (3,3)	2.0%	0.45	79.5%	3.9%	0.063	90.8%

footprint were more advantageous in SD007 vs SD008. Mean differences were consistently positive suggesting that, within this range of inter-contact densities, adding more channels within a given footprint does not reduce state estimation performance which is intuitive and consistent with modeling results. This is the first time that 400 μm grids have been shown to significantly outperform larger pitch grids placed on human cortex; 400 μm pitch is 5x smaller than previous work (Muller et al., 2016a). Note, that (Muller et al., 2016a) only directly sub-sampled the original grid roughly similar to fixing area, but did not show results for fixing channel count. In many practical situations though, the number of channels is a limiting factor, and so an important density comparison is to vary pitch while controlling for number of channels. Due to the number of bad channels within our microgrid, particularly for SD007, we were not able to perform this analysis in an unbiased fashion as there tended to be a larger percentage of good channels for the denser virtual grids for this particular comparison (Fig. S8). Although the results of this analysis will likely overestimate the performance of denser, the results may still be informative. When controlling for channels in both subjects, μECoG grids with a smaller pitch did not significantly differ from their larger pitch counterparts except once. In fact, we observed negative means suggesting that higher density grids may underperform their lower density counterparts when controlling for channel count (Fig. S7). Taken together with the bias, we can conclude that high density grids certainly have not outperformed lower density grids while controlling for channel count.

The empirical results of two subjects provide an existence proof that 400 μm grids can outperform lower density grids with respect to neural state estimation. However, the extent to which these results generalize to a wider range of neural state estimation problems, cortical areas, and subjects, will require a substantially expanded clinical research trial with high-density/low-impedance electrode technologies that are currently not available commercially. Thus, these empirical findings are not intended to validate the presented modeling framework. The purpose of the model is to provide insight into potential circumstances under which high density grids might outperform low density grids and to utilize these insights towards aiding in the interpretation of these and future empirical findings. More sophisticated models will need to be developed to precisely model real data.

In evaluating the empirical results, it is important to note that common average reference (CAR), although intended to improve single channel signal fidelity, can have deleterious effects on signal quality. Ideally, CAR is applied to a set of signals contaminated with identical artifact such as 60 Hz artifacts, in which case CAR will eliminate it. But, if only few channels contain artifacts, the artifacts will be introduced to all other signals. This is likely not the case for either subject as applying CAR does not reduce decoding performance (Fig. 5) or visibly contaminate channels in the HFB trial averages (Figs. S3–S4). On the other hand, if half of signals recorded from a grid are similar to each other, and the other half are also similar to each other, but different from the first half, then CAR will introduce many interdependencies/correlations. This is likely not the case for the analyses conducted for SD007 and SD008 since the HFB spatial response remains focal after CAR (Fig. 5, S3-S4). Nevertheless, it is important to understand the implications of CAR, especially for μECoG since it can drastically alter the signals and their interpretation.

The choice of learning algorithm used to assess grid performance is important. A poor choice that is not robust to high dimensional datasets will likely underperform, due to overfitting. We chose ELR, because it performs feature selection while optimizing parameters, making it robust to high dimensional datasets. Furthermore, ELR manages highly correlated variables well by promoting a group of correlated variables to be either all in or out (Zou and Hastie, 2005).

One limitation of these experiments was the small coverage area of the μECoG probe, which was approximately 3 mm by 3 mm. The small coverage area makes it difficult to align the recording region to the brain regions of interest. This is illustrated in SD007, where the HFB response only starts to become apparent on the left edge of the grid. If a larger grid was used, we may have been able to measure the full extent of the spatial response and be able to center the virtual grids over regions of peak activation for better grid comparison. A major challenge to increasing the area for such small pitch grids is scaling connectors and amplification circuits. However, we anticipate that advances in technology will make higher channel count systems cheaper and easier to access (Hermiz et al., 2016; Insanally et al., 2016; Trumpis et al., 2017), thus making higher density probes more attractive to use.

Conclusion

Here we report the first instance of 400 μm pitch grids outperforming lower density grids in estimating cognitive neural states from humans. We also explored how signal and noise spatial properties affect the performance gap between low and high-density grids by developing an illustrative model, which we found to be consistent with our empirical results. In the future, we plan to add more channels to increase the coverage area, extend the presented model and explore other signal features. Increasing channel count and footprint of the μECoG will be important for fully exploring possible advantages over ECoG. The presented model could evolve to become an important piece in a design method for μECoG probes. The design method could take as input specifications such as desired classification accuracy, channel count and expected characteristic lengths and output the optimal pitch for specific applications. Finally, finer spatial scales may allow us to measure novel neural dynamics such as wave propagation or spiking activity. We plan to explore other signal features to potentially uncover novel neural dynamics only visible at the micrometer scale.

Acknowledgements

We would like to acknowledge James Proudfoot from the Altman Clinical and Translational Research Institute, Biostatistics team for his advice regarding statistical analyses. This work was graciously supported by the Center for Brain Activity Mapping (CBAM) at UC San Diego. S.A.D. and V.G. acknowledge faculty start-up support from the Department of Electrical and Computer Engineering at UC San Diego. S.A.D. acknowledges partial support from the NSF No. ECCS-1351980. V.G. acknowledges partial support from University of California Multicampus Research Programs and Initiatives (UC MRPI) No. MR-15-328909. E.H. acknowledges partial support from the Office of Naval Research No. N00014-13-1-0672.

Conflicts of interest

No competing interests.

Appendix A. Supplementary data

Supplementary data related to this article can be found at https://doi.

org/10.1016/j.neuroimage.2018.04.027.

References

Blakely, T., Miller, K.J., Rao, R.P., Holmes, M.D., Ojemann, J.G., 2008. Localization and classification of phonemes using high spatial resolution electrocorticography (ECoG) grids. Conf. Proc. Annu. Int. Conf. IEEE Eng. Med. Biol. Soc. IEEE Eng. Med. Biol. Soc. Annu. Conf. 4964–4967. https://doi.org/10.1109/IEMBS.2008.4650328, 2008.

Bleichner, M.G., Freudenburg, Z.V., Jansma, J.M., Aarnoutse, E.J., Vansteensel, M.J., Ramsey, N.F., 2016. Give me a sign: decoding four complex hand gestures based on high-density ECoG. Brain Struct. Funct. 221 https://doi.org/10.1007/s00429-014-0902-x.

Branco, M.P., Freudenburg, Z.V., Aarnoutse, E.J., Bleichner, M.G., Vansteensel, M.J., Ramsey, N.F., 2016. Decoding hand gestures from primary somatosensory cortex using high-density ECoG. Neuroimage 147, 130–142. https://doi.org/10.1016/j.neuroimage.2016.12.004.

Castagnola, E., Maiolo, L., Maggiolini, E., Minotti, A., Marrani, M., Maita, F., Pecora, A., Angotzi, G.N., Ansaldo, A., Boffini, M., Fadiga, L., Fortunato, G., Ricci, D., 2015. PEDOT-cnt-coated low-impedance, ultra-flexible, and brain-conformable micro-ECoG arrays Elisa. IEEE Trans. Neural Syst. Rehabil. Eng. 23, 342–350.

Chang, E.F., 2015. Towards large-scale, human-based, mesoscopic neurotechnologies. Neuron 86, 68–78. https://doi.org/10.1016/j.neuron.2015.03.037.

Crone, N.E., Boatman, D., Gordon, B., Hao, L., 2001. Induced electrocorticographic gamma activity during auditory perception. Clin. Neurophysiol. 112, 565–582. https://doi.org/10.1016/S1388-2457(00)00545-9.

Crone, N.E., Crone, N.E., Miglioretti, D.L., Miglioretti, D.L., Gordon, B., Gordon, B., Sieracki, J.M., Sieracki, J.M., Wilson, M.T., Wilson, M.T., Uematsu, S., Uematsu, S., Lesser, R.P., Lesser, R.P., 1998. Functional mapping of human sensorimotor cortex with electrocorticographic spectral analysis. I. Alpha and beta event-related desynchronization. Brain 121 (Pt 1), 2271–2299. https://doi.org/10.1093/brain/121.12.2271.

Fang, H., Yu, K.J., Gloschat, C., Yang, Z., Song, E., Chiang, C.-H., Zhao, J., Won, S.M., Xu, S., Trumpis, M., Zhong, Y., Han, S.W., Xue, Y., Xu, D., Choi, S.W., Cauwenberghs, G., Kay, M., Huang, Y., Viventi, J., Efimov, I.R., Rogers, J.A., 2017. Capacitively coupled arrays of multiplexed flexible silicon transistors for long-term cardiac electrophysiology. Nat. Biomed. Eng. 1, 38. https://doi.org/10.1038/s41551-017-0038.

Flinker, A., Chang, E.F., Barbaro, N.M., Berger, M.S., Knight, R.T., 2011. Sub-centimeter language organization in the human temporal lobe. Brain Lang. 117, 103–109. https://doi.org/10.1016/j.bandl.2010.09.009.

Flint, R.D., Rosenow, J.M., Tate, M.C., Slutzky, M.W., 2017. Continuous decoding of human grasp kinematics using epidural and subdural signals. J. Neural Eng. 14 https://doi.org/10.1088/1741-2560/14/1/016005, 16005.

Freeman, W.J., Rogers, L.J., Holmes, M.D., Silbergeld, D.L., 2000. Spatial spectral analysis of human electrocorticograms including the alpha and gamma bands. J. Neurosci. Methods 95, 111–121. https://doi.org/10.1016/S0165-0270(99)00160-0.

Ganji, M., Kaestner, E., Hermiz, J., Rogers, N., Tanaka, A., Cleary, D., Lee, S.H., Snider, J., Halgren, M., Cosgrove, G.R., Carter, B.S., Barba, D., Uguz, I., Malliaras, G.G., Cash, S.S., Gilja, V., Halgren, E., Dayeh, S.A., 2017. Development and translation of PEDOT: PSS microelectrodes for intraoperative monitoring. Adv. Funct. Mat. https://doi.org/10.1002/adfm.201700232, 1700232.

Hermiz, J., Rogers, N., Kaestner, E., Ganji, M., Cleary, D., Snider, J., Barba, D., Dayeh, S., Halgren, E., Gilja, V., 2016. A clinic compatible, open source electrophysiology system. In: Eng. Med. Biol. Soc. (EMBC), 2016 IEEE 38th Annu. Int. Conf, pp. 4511–4514. https://doi.org/10.1109/EMBC.2016.7591730.

Horton, J.C., Adams, D.L., 2005. The cortical column: a structure without a function. Philos. Trans. R. Soc. B Biol. Sci. 360, 837–862. https://doi.org/10.1098/rstb.2005.1623.

Hwang, E.J., Andersen, R.A., 2013. The utility of multichannel local field potentials for brain-machine interfaces. J. Neural Eng. 10 https://doi.org/10.1088/1741-2560/10/4/046005, 46005.

Insanally, M., Trumpis, M., Wang, C., Chiang, C.-H., Woods, V., Palopoli-Trojani, K., Bossi, S., Froemke, R.C., Viventi, J., 2016. A low-cost, multiplexed μECoG system for high-density recordings in freely moving rodents. J. Neural Eng. 13 https://doi.org/10.1088/1741-2560/13/2/026030, 26030.

Jiang, T., Jiang, T., Wang, T., Mei, S., Liu, Q., Li, Y., Wang, X., Prabhu, S., Sha, Z., Ince, N.F., 2017. Characterization and decoding the spatial patterns of hand extension/flexion using high-density ECoG. IEEE Trans. Neural Syst. Rehabil. Eng. 4320 https://doi.org/10.1109/TNSRE.2016.2647255, 1–1.

Kaiju, T., Doi, K., Yokota, M., Watanabe, K., Inoue, M., Ando, H., Takahashi, K., Yoshida, F., Hirata, M., Suzuki, T., 2017. High spatiotemporal resolution ECoG recording of somatosensory evoked potentials with flexible micro-electrode arrays. Front. Neural Circ. 11, 20. https://doi.org/10.3389/fncir.2017.00020.

Kellis, S., Miller, K., Thomson, K., Brown, R., House, P., Greger, B., 2010. Decoding spoken words using local field potentials recorded from the cortical surface. J. Neural Eng. 7 https://doi.org/10.1088/1741-2560/7/5/056007, 56007.

Kellis, S., Sorensen, L., Darvas, F., Sayres, C., Neill, K.O., Brown, R.B., House, P., Ojemann, J., Greger, B., 2016. Clinical Neurophysiology Multi-scale analysis of neural activity in humans : implications for micro-scale electrocorticography. Clin. Neurophysiol. 127, 591–601. https://doi.org/10.1016/j.clinph.2015.06.002.

Kellis, S.S., House, P.A., Thomson, K.E., Brown, R., Greger, B., 2009. Human neocortical electrical activity recorded on nonpenetrating microwire arrays: applicability for neuroprostheses. Neurosurg. Focus 27, E9. https://doi.org/10.3171/2009.4.FOCUS0974.

Khodagholy, D., Doublet, T., Gurfinkel, M., Quilichini, P., Ismailova, E., Leleux, P., Herve, T., Sanaur, S., Bernard, C., Malliaras, G.G., 2011. Highly conformable conducting polymer electrodes for in vivo recordings. Adv. Healthc. Mater 23, 268–272. https://doi.org/10.1002/adma.201102378.

Khodagholy, D., Gelinas, J.N., Thesen, T., Doyle, W., Devinsky, O., Malliaras, G.G., Buzsáki, G., 2014. NeuroGrid ;: recording action potentials from the surface of the brain. Nat. Neurosci. https://doi.org/10.1038/nn.3905.

Khodagholy, D., Gelinas, J.N., Zhao, Z., Yeh, M., Long, M., Greenlee, J.D., Doyle, W., Devinsky, O., Buzsáki, G., 2016. Organic electronics for high-resolution electrocorticography of the human brain. Sci. Adv. 1–9.

Ledochowitsch, P., Koralek, A.C., Moses, D., Carmena, J.M., Maharbiz, M.M., 2013. Sub-mm functional decoupling of electrocortical signals through closed-loop BMI learning. Conf. Proc. Annu. Int. Conf. IEEE Eng. Med. Biol. Soc. IEEE Eng. Med. Biol. Soc. Annu. Conf. 2013, 5622–5625. https://doi.org/10.1109/EMBC.2013.6610825.

Leuthardt, E.C., Freudenberg, Z., Bundy, D., Roland, J., 2009. Microscale recording from human motor cortex: implications for minimally invasive electrocorticographic brain-computer interfaces. Neurosurg. Focus 27, E10. https://doi.org/10.3171/2009.4.FOCUS0980.

Ludwig, K.A., Miriani, R.M., Langhals, N.B., Joseph, M.D., Anderson, D.J., Kipke, D.R., 2009. Using a common average reference to improve cortical neuron recordings from microelectrode arrays. J. Neurophysiol. 101, 1679–1689. https://doi.org/10.1152/jn.90989.2008.

Maharbiz, M.M., Muller, R., Alon, E., Rabaey, J.M., Carmena, J.M., 2017. Reliable next-generation cortical interfaces for chronic brain–machine interfaces and neuroscience. Proc. IEEE 105, 73–82. https://doi.org/10.1109/JPROC.2016.2574938.

Miller, K.J., Leuthardt, E.C., Schalk, G., Rao, R.P.N., Anderson, N.R., Moran, D.W., Miller, J.W., Ojemann, J.G., 2007. Spectral changes in cortical surface potentials during motor movement. J. Neurosci. 27, 2424–2432. https://doi.org/10.1523/JNEUROSCI.3886-06.2007.

Muller, L., Felix, S., Shah, K.G., Lee, K., Pannu, S., Chang, E.F., 2016a. Thin-film, high-density micro-electrocorticographic decoding of a human cortical gyrus. In: Eng. Med. Biol. Soc. (EMBC), 2016 IEEE 38th Annu. Int. Conf, pp. 1528–1531. https://doi.org/10.1109/EMBC.2016.7591001.

Muller, L., Hamilton, L.S., Edwards, E., Bouchard, K.E., Chang, E.F., 2016b. Spatial resolution dependence on spectral frequency in human speech cortex electrocorticography. J. Neural Eng. 13 https://doi.org/10.1088/1741-2560/13/5/056013, 56013.

Qian, J., Hastie, T., Friedman, J., Tibshirani, R., Simon, N., 2013. Glmnet for Matlab, 2013. http//www. stanford. edu/~ Hast.

Rockland, 2010. Five points on columns. Front. Neuroanat. https://doi.org/10.3389/fnana.2010.00022.

Slutzky, M.W., Jordan, L.R., Krieg, T., Chen, M., Mogul, D.J., Miller, L.E., 2010. Optimal spacing of surface electrode arrays for brain-machine interface applications. J. Neural Eng. 7 https://doi.org/10.1088/1741-2560/7/2/026004, 26004.

Toda, H., Suzuki, T., Sawahata, H., Majima, K., Kamitani, Y., Hasegawa, I., 2011. Simultaneous recording of ECoG and intracortical neuronal activity using a flexible multichannel electrode-mesh in visual cortex. Neuroimage 54, 203–212. https://doi.org/10.1016/j.neuroimage.2010.08.003.

Travis, K.E., Leonard, M.K., Chan, A.M., Torres, C., Sizemore, M.L., Qu, Z., Eskandar, E., Dale, A.M., Elman, J.L., Cash, S.S., Halgren, E., 2013. Independence of early speech processing from word meaning. Cereb. Cortex 23, 2370–2379. https://doi.org/10.1093/cercor/bhs228.

Trumpis, M., Insanally, M., Zou, J., ElSharif, A., Ghomashchi, A., Artan, N.S., Froemke, R., Viventi, J., 2017. A low-cost, scalable, current-sensing digital headstage for high channel count μECoG. J. Neural Eng. https://doi.org/10.1088/1741-2552/aa5a82.

Uguz, I., Ganji, M., Hama, A., Tanaka, A., Inal, S., Youssef, A., Owens, R.M., Quilichini, P.P., Ghestem, A., Bernard, C., Dayeh, S.A., Malliaras, G.G., 2016. Autoclave sterilization of PEDOT: PSS electrophysiology devices. Adv. Healthc. Mater 1–5. https://doi.org/10.1002/adhm.201600870.

Viventi, J., Kim, D.-H., Vigeland, L., Frechette, E.S., Blanco, J.A., Kim, Y.-S., Avrin, A.E., Tiruvadi, V.R., Hwang, S.-W., Vanleer, A.C., Wulsin, D.F., Davis, K., Gelber, C.E., Palmer, L., Van der Spiegel, J., Wu, J., Xiao, J., Huang, Y., Contreras, D., Rogers, J.A., Litt, B., 2011. Flexible, foldable, actively multiplexed, high-density electrode array for mapping brain activity in vivo. Nat. Neurosci. 14, 1599–1605. https://doi.org/10.1038/nn.2973.

Wang, P.T., King, C.E., McCrimmon, C.M., Lin, J.J., Sazgar, M., Hsu, F.P.K., Shaw, S.J., Millet, D.E., Chui, L.A., Liu, C.Y., Do, A.H., Nenadic, Z., 2016. Comparison of decoding resolution of standard and high-density electrocorticogram electrodes. J. Neural Eng. 13 https://doi.org/10.1088/1741-2560/13/2/026016, 26016.

Zou, H., Hastie, T., 2005. Regularization and variable selection via the elastic net. J. R. Stat. Soc. Ser. B Stat. Methodol. 67, 301–320. https://doi.org/10.1111/j.1467-9868.2005.00503.x.